

**Timing and composition of continental volcanism at Harrat Hutaymah,
western Saudi Arabia**

Tyler D. Schlieder¹, Robert A. Duncan^{1,2}, Carl R. Thornber³ and Abdullah M. Al-Amri²

¹ College of Earth, Ocean, and Atmospheric Sciences, Oregon State University, Corvallis, OR 97333 USA

² Department of Geology and Geophysics, King Saud University, Riyadh, KSA

³ U.S. Geological Survey, Cascades Volcano Observatory, Vancouver, WA USA

Abstract

Harrat Hutaymah is an alkali basaltic, continental volcanic field in north-central Saudi Arabia. Lava flow compositions in the region include alkali olivine basalts and basanites, which contrast with the predominantly tholeiitic basalts bordering the Red Sea. These lava flows commonly contain a range of crustal and lithospheric xenoliths. Previous radiometric dating at this harrat (a single K-Ar age; 1.8 Ma) is suspiciously old given the common occurrence of xenolithic material in the lava flows and the field measurement of only normal magnetic polarity (i.e. Brunhes interval, ≤ 780 ka). We report new age determinations by the ^{40}Ar - ^{39}Ar incremental step heating method, all younger than ~ 850 Ka and major, trace and rare earth element compositions to better constrain the time frame of volcanism and chemical variation at Harrat Hutaymah. We use these new data to model the depth and degree of partial melting beneath Harrat Hutaymah (65-80 km; $\sim 5\%$). This compares with contemporaneous Harrat Rahat (20-40 km; 10-15%), part of the central north-south trending larger volcanic fields, Harrat Lunayyir (60-75 km; 7-12%), 100 km east of the Red Sea, and the Red Sea spreading axis (0-10 km; 25%). This variability in mantle melting can be explained by regional

lithospheric extension and mantle decompression melting coupled with northward asthenospheric flow from the Afar hot spot.

Introduction

The Harrat Province

One of the largest alkali basalt provinces in the world (area: 180,000 km²) is located in the western part of the Arabian Peninsula (**Figure 1**). These extensive Cenozoic basaltic lava fields (“harrats”) erupted from N-S oriented volcanic centers that lie within 300 km of the NW-trending eastern margin of the Red Sea. The origin of these fields is partially related to regional extension of thick, Pan-African craton that began ~30 Ma, but there is no reflection of these volcanic centers on the eastern African plate margin (Bohannon et al., 1989). In contrast with tholeiitic basalts of the Red Sea spreading system, lava compositions in the region include alkali ol-basalts, ol-transitional basalts, hawaiites, with minor more evolved compositions, and have been erupted through the Proterozoic continental shield of the Saudi Arabian Peninsula. In the harrat province, early Red Sea-parallel volcanism (>12 Ma) was dominated by tholeiitic to transitional compositions, but has become more alkalic with younger, N-S oriented, eruptive centers (<12 Ma). A prominent volcanic structure, the Makkah-Madinah-Nafud (MMN) line, appears to coincide with the axis of uplift of the Arabian shield, beginning ~15 Ma.

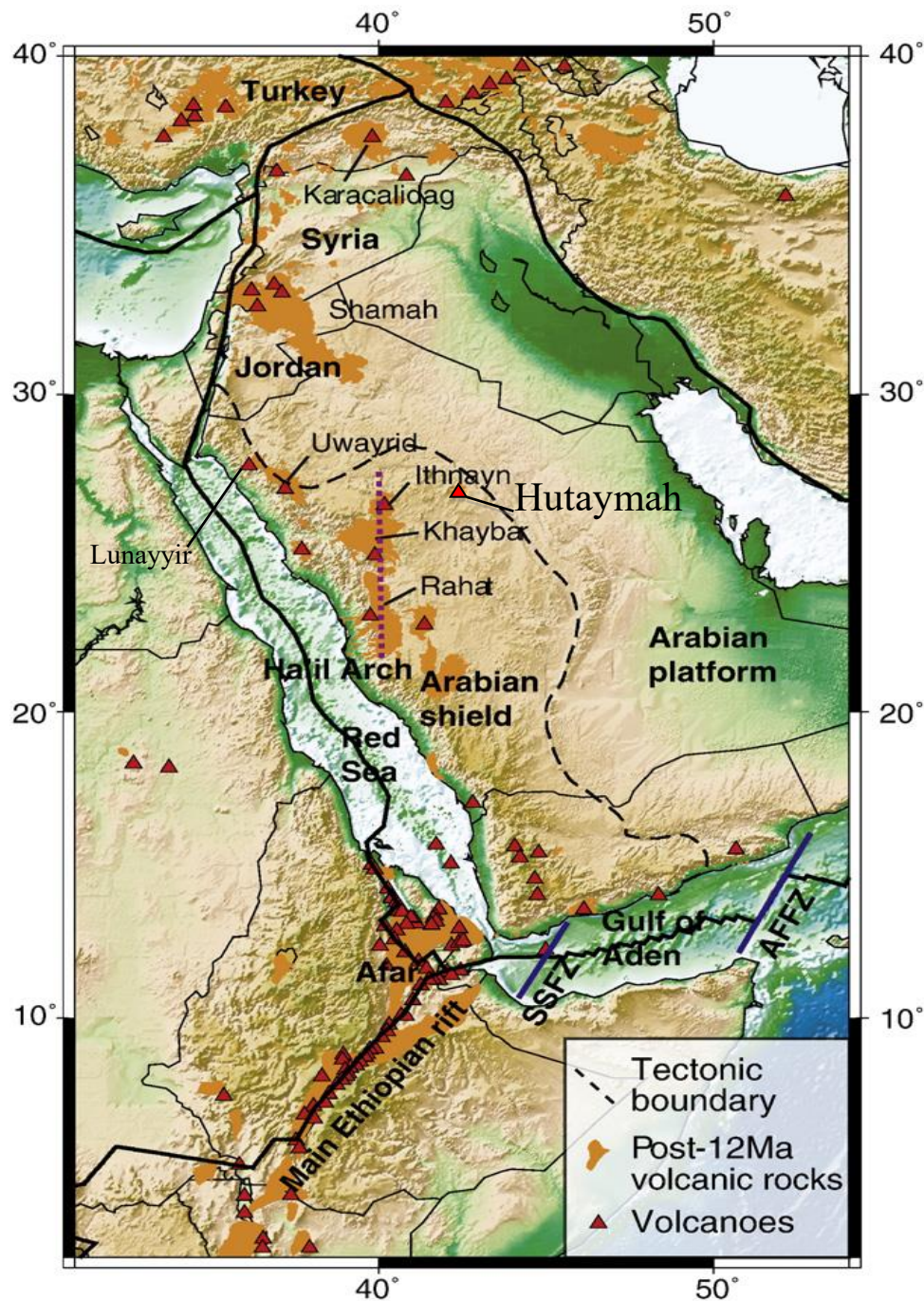


Figure 1. Location map for volcanic fields (‘harrats’) in western Saudi Arabia (Chang and van der Lee, 2011). Individual harrats lie within 300 km of the Red Sea margin, but eruptive centers/fissures are aligned predominantly N–S. The most voluminous provinces fall within the region indicated by dotted red line (Ha’il Arch), also called the Makkah–Medinah–Nafud (MMN) lineament. Harrat Hutaymah is a relatively small province that lies east the MMN line.

Harrat Hutaymah

Harrat Hutaymah (**Figure 2**), one of the smallest and youngest harrats with volcanic deposits covering $\sim 900 \text{ km}^2$, is the eastern most Harrat, $\sim 500 \text{ km}$ from the Red Sea axis (Thornber, 1992). Previous work at Hutaymah, which includes geochemical and petrologic studies and K-Ar age determinations that yield ages from 0.1 Ma to 2.65 Ma (Thornber, 1992 and Pallister, 1984), reveal that Harrat Hutaymah is dominated by a compositionally narrow range of alkaline basalts from basanite to trachy-basalt that erupted from 15 main centers. Hutaymah is unique compared to other Arabian harrats in the unusual abundance of explosive volcanism and mantle derived xenolithic material (Thornber, 1992). Previous models for the petrogenesis of Harrat Hutaymah, and the Harrat province as a whole, attribute the presence of volcanism to simple decompression melting related to the Red Sea Rift.

A recent study of Harrat Lunayyir, located west of Harrat Hutaymah, by Duncan and Al-Amri (2013) suggests that previous K-Ar ages reported at many harrats may be inaccurate. This study also proposes a model for the petrogenesis of the harrat region. Duncan and Al-Amri's (2013) model explains the variable timing and composition observed throughout the region with lithospheric thinning and asthenospheric flow from the Afar hot spot. The location of Harrat Hutaymah on the eastern edge of the harrat province, the extensive geochemical work reported by Thornber (1992), and the poorly constrained K-Ar ages make Hutaymah an ideal location to test the validity of these claims, with further geochemical analysis and new age determinations using high precision ^{40}Ar - ^{39}Ar geochronology. These new data, in combination with previous data reported for Harrat Lunayyir (Duncan and Al-Amri, 2013), Harrat Rahat (Moufti et al.,

2013), and the Red Sea (Kelley et al. 2013, and Vlastelic et al., 1998) will be analyzed in order to test the validity of the two proposed hypotheses for the petrogenesis of Harrat Hutaymah:

- 1) Hutaymah volcanism is the result of simple decompression melting related to the rifting of the Red Sea.
- 2) Hutaymah volcanism is the result of regional lithospheric extension and mantle decompression melting coupled with northward asthenospheric flow from the Afar hot spot.

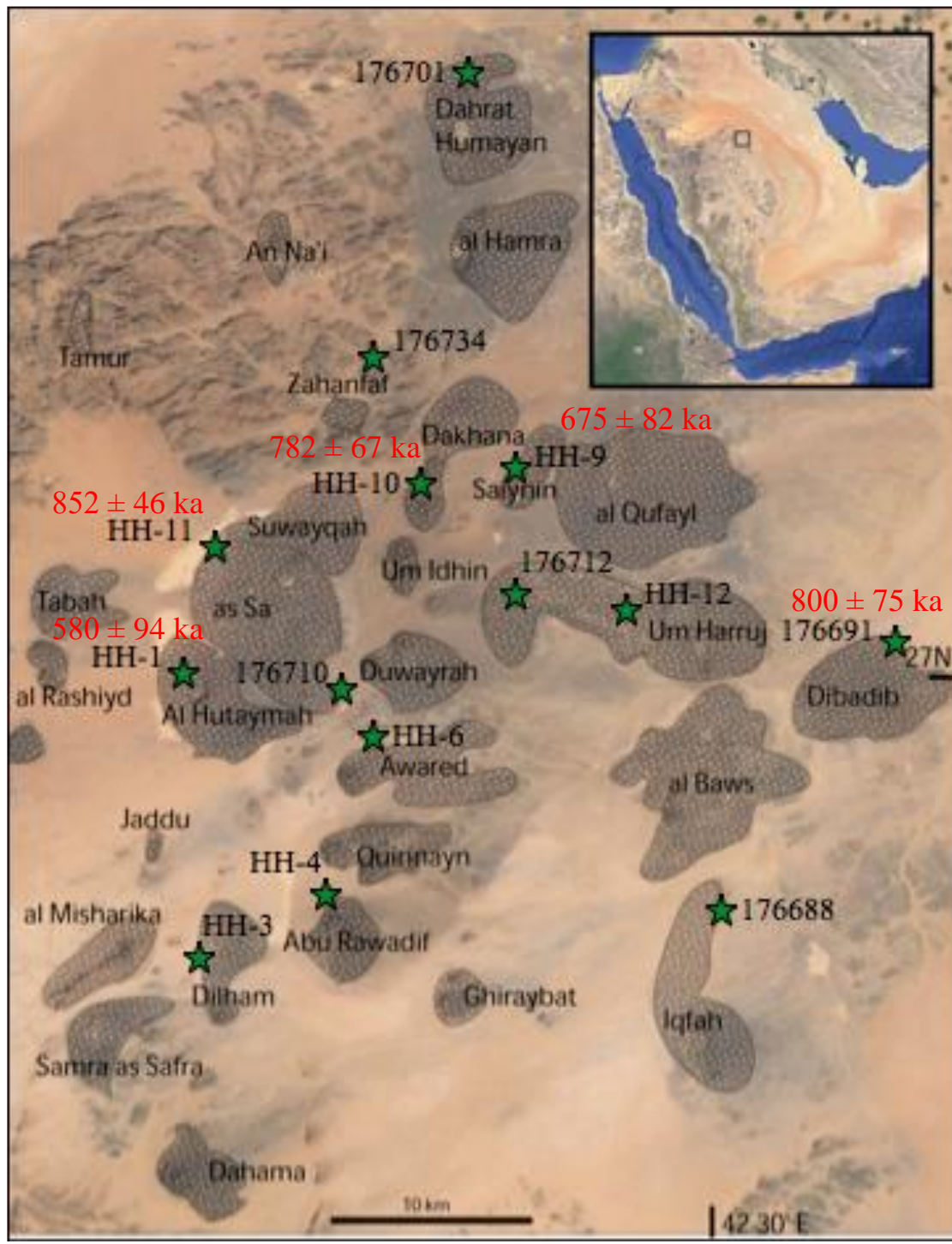


Figure 2. Harrat Hutaymah, western Saudi Arabia. The various volcanic fields are labeled on the map, and the green stars mark the location of samples collected for geochemical analysis, $^{40}\text{Ar}/^{39}\text{Ar}$ ages for five samples are reported in red.

Volcanology

Harrat Hutaymah volcanism is restricted to a narrow range of alkaline mafic lava compositions that cover a relatively small area (~900 km²) compared to other Arabian harrats (Thornber, 1992). It was named after one of the most prominent volcanic crater in the area, *Al Hutaymah*, a large ~1 km diameter, 300 m deep vent, located in the west central area of the volcanic field (Bramkamp et al., 1963 and Thornber, 1992). *Al Hutaymah* is one of 15 main explosive centers distributed throughout the harrat. In addition to the large craters, Hutaymah presents an unusual abundance of tuff rings and maars, suggesting a higher concentration of violently explosive activity. This has been attributed to interactions with water, resulting in phreatomagmatic style eruptions (Thornber, 1992)

The intense concentration of explosive activity at Hutaymah is reflected in the abundant tephra deposits of variable crater morphology (Thornber, 1992). Isolated maars (craters rimmed by tuff rings) can be found at *Al Hutaymah*, *Thbah*, *Tamar*, *An Nai*, and *Harrat Al Hamra*. Isolated tuff ring rimmed craters that have been largely in-filled by quaternary alluvium are found at *Samra as Safra*, *Harrat al Dibadib*, *Harrat Humayan*, and *Harrat Dakhana*, and with grouped vents of similar morphology at *Jabal Dilham*, *Jabal Umm Haraj*, *Jabal Duwayrah*, *North Harrat as Sa*, *Jabal Al Qufayl*, and *Harrat Siaynin* (Thornber, 1992). Commonly reworked tephra can be found radially distributed from the tuff rings, covering an area of 10-60 km². Large lava flows up to 60 km² and 40 m thick overlie nested tuff rings at *Harrat Al Jaddir*, *Harrat Al Hamra*, and *Harrat as Sa*, and the inverse relationship, tuff-ring tephra superimposed over coherent flows, can be viewed in maar walls at *Al Hutaymah* and *Jabal Iqfah* (Thornber, 1992). Approximately

85 small alkali basaltic cinder/spatter cones (<1 km diameter) and fissure events (<1-2 km length) produced scoria and small a'a flows (w/ minor pahoehoe) (Thornber, 1992).

A defining characteristic of Hutaymah volcanism is the abundance of ultramafic xenoliths and megacrysts distributed throughout the tephra, flows, and spatter cones; likely sourced from the lower crust or upper mantle (Thornber, 1990). Collectively, these isolated and grouped cones, maars, tuff-rings, and elongate fissure eruptions define the eruptive characteristics of the entire harrat (Thornber, 1992).

METHODS

Fifty-seven samples collected from Harrat Hutaymah by Dr. Robert A. Duncan and Dr. Carl Thornber form the basis of this research. Samples were examined in hand sample and thin section (HH-1 to HH-12) and divided into groups based on spatial distribution, texture, and mineralogy for dating and geochemical analysis. Samples unsuitable for age determinations based on extensive alteration were excluded from further analysis. Ideal samples were well-crystallized with an absence of interstitial glass, aphyric to sparsely phyrlic, and contained no visible xenoliths.

Major and trace element data were collected for select samples using Instrumental Neutron Activation Analysis (INAA) (Thornber, 1992). Additional major element data were collected using X-ray fluorescence (XRF) at the Washington State University Geoanalytical Lab. Trace element and rare earth data were collected using INAA (Thornber, 1992) and inductively coupled plasma mass spectrometry (ICP-MS) at the Washington State University Geoanalytical Lab.

Age determinations of groundmass separates were performed at Oregon State University using standard ^{40}Ar - ^{39}Ar incremental heating methods using biotite flux monitor FCT-3 (28.02 Ma). Samples were crushed, sieved, washed, and subjected to mild acid leaching with HCl and HNO₃ prior to irradiation in the OSU TRIGA reactor. Argon isotope compositions of irradiated samples were determined using the Thermo Scientific Model ARGUS VI multi-collector with five fixed Faraday detectors, attached to an all-metal extraction line. Samples were heated using an air-cooled Synrad 25W CO₂ laser capable of moving at speeds up to 300 in/s to ensure even heating of the entire sample

being analyzed. Incremental step heating, using 16 heating steps, and isochron ages were calculated for each sample using the ArArCALC v2.5.2 software package (Koppers, 2002). The new high precision ARGUS VI allows for accurate age determinations on samples otherwise too young for the older Mass Analyzer Products (MAP) 215-50 mass spectrometer.

Parental melt evolution was modeled using the MELTS software package (Ghiorso and Sack, 1995). Using thermodynamic properties MELTS models the evolution of magmas in a series of steps of varying temperature and/or pressure, and characterize equilibrium and fractional crystallization trends by producing a liquid line of descent. Calculations were done beginning from the liquidus and cooling at 2 °C temperature intervals at constant pressure. Oxygen fugacity was buffered at the quartz-fayalite–magnetite buffer (QFM). The initial magma composition used in the model is found in **Table 5**. This starting composition was estimated on the basis of Mg#, MgO content, and petrographic inspection in order to estimate the most primitive composition while avoiding Mg enrichment from olivine accumulation.

In order to determine the melting conditions and mantle source composition that formed primary Hutaymah magmas, a batch-melting model was developed. This model calculates the concentration of rare earth elements (REEs) in a magma derived from a given mantle source at variable degrees of partial melting. Partition coefficients and both primitive and depleted mantle source compositions (**Table 1**) have been adapted from Gurenko and Chaussidon (1995).

Element	Primitive Mantle Source	Depleted Mantle Source (ppm)	Partition Coefficients					
			Ol	Opx	Cpx	Pl	Sp	Ga
La	0.69	0.31	3.10E-05	4.40E-05	5.36E-02	1.21E-01	6.00E-04	1.00E-03
Ce	1.78	0.95	1.00E-04	1.40E-04	8.58E-02	9.68E-02	6.00E-04	4.00E-03
Nd	1.35	0.86	4.20E-04	5.20E-04	1.87E-01	6.52E-02	6.00E-04	5.70E-02
Sm	0.44	0.32	1.10E-03	1.60E-03	2.91E-01	5.55E-02	6.00E-04	6.25E-01
Eu	0.17	0.13	7.50E-04	6.40E-04	3.50E-01	6.34E-01	6.00E-04	1.00E+00
Dy	0.74	0.64	1.40E-03	8.40E-03	4.42E-01	2.85E-02	1.50E-03	2.00E+00
Er	0.48	0.35	1.30E-02	1.70E-02	3.87E-01	1.63E-02	3.00E-03	3.00E+00
Yb	0.49	0.43	3.00E-02	3.30E-02	4.30E-01	1.12E-02	4.50E-03	4.00E+00
Ba	6.99	1.19	3.20E-04	1.70E-04	6.80E-04	6.88E-01	0.00E+00	1.00E-05
Nb	0.71	0.28	5.00E-05	1.40E-03	7.70E-03	3.33E-01	1.00E-02	1.75E-02
Sr	21.1	13.2	1.50E-03	5.10E-04	1.28E-01	2.10E+00	0.00E+00	1.40E-02
Zr	11.2	8.4	5.80E-04	3.30E-03	1.23E-01	9.00E-04	7.00E-02	5.05E-01
Ti	1300	1090	1.40E-02	8.20E-02	3.80E-01	4.68E-02	1.50E-01	6.30E-01
Y	4.6	4.1	9.40E-03	9.60E-03	4.67E-01	1.15E-02	4.00E-03	4.20E+00
V	82.0	53.7	3.00E-01	6.10E-01	3.10E+00	2.70E-02	4.50E-03	3.60E+00

Table 1. Partition coefficients, primitive mantle source, and depleted mantle source compositions used for REE modeling, adapted from Gurenko and Chaussidon (1995).

RESULTS

Petrography

Of the twelve samples examined petrographically, eleven have clearly identifiable mineralogies. Phenocryst concentration varies widely from 15% to 85%, but averages ~30-35%. Samples are dominantly olivine phyric to microphyric (40-85% olivine) with subhedral to euhedral olivine (0.1 to 3mm) in an aphanitic groundmass of fine plagioclase laths and interstitial olivine and pyroxene. Hexagonal, rounded, and hopper morphologies are common in olivine, and most crystals are at least partially altered to iddingsite. When possible, forsterite content was estimated using 2V angle, ranging from Fo₈₀ to Fo₈₅. Pyroxenes, mainly augite (0.1 to 1mm), do not exceed 10% of the total phenocryst population, and are unsuitable for an estimate of enstatite content. Plagioclase is typically confined to fine grained laths in the groundmass, but in four samples large (up to 3mm) plagioclase crystals are present. In these cases the plagioclase is highly sieved with large embayments along the rims. The majority of plagioclase is too fine to estimate anorthite content, but in large zoned and sieved plagioclase from HH-11 the composition was estimated to be An₄₅ to An₇₀. Minor opaque minerals, likely spinel (0.25mm), are ubiquitous at ~5%. Samples are commonly diktytaxitic, and less commonly pilotaxitic. Glomerocrysts of large plagioclase phenocrysts are abundant in some samples, and commonly occur with quartz xenoliths. Nearly all samples exhibit an aphanitic glassy groundmass ranging from slightly vesicular to non-vesicular with the exception of sample HH-11 that is almost entirely crystalline.

Geochronology

^{40}Ar - ^{39}Ar ages obtained for eight samples are summarized in **Table 2**. Reliable plateau ages range from 500 to 852 Ka, with two samples failing to produce a plateau. These new ages are considerably less variable than previous K/Ar ages (0.1 to 2.65 Ma, Thornber, 1992), and are significantly younger than the most recent K/Ar age of 1.84 ± 0.05 Ma reported by Pallister (1984). Representative age spectra can be seen in **Figure 3**.

Sample	Total Fusion (Ma)	2σ error (ka)	Plateau Age (ka)	2σ error (ka)	N	MSWD	Isochron Age (ka)	2σ error (ka)	$^{40}\text{Ar}/^{36}\text{Ar}$ initial	2σ error
HH-1	664	108	580	94	16/16	1.20	334	212	297	1
HH-3	1910	100	<i>not developed</i>				<i>not developed</i>			
HH-4	2190	90	<i>not developed</i>				<i>not developed</i>			
HH-6	590	2130	500	1930	16/16	0.20	980	2770	295	2
HH-9	936	140	675	82	12/16	0.9	574	205	296	1
HH-10	782	77	782	67	16/16	0.97	714	140	297	3
HH-11	852	39	852	46	14/16	1.75	760	113	297	2
HH-12	875	74	800	75	33/33	2.58	774	185	296	1

Table 2. Ages calculated using biotite monitor FCT-3 (28.02 Ma, Renne et al., 1998) and the total decay constant $\lambda = 5.530\text{E}-10/\text{yr}$. N is the number of heating steps (defining plateau/total); MSWD is an F-statistic that compares the variance within step ages with the variance about the plateau age. J combines the neutron fluence with the monitor age. Preferred ages are shown in bold; italics indicate sample with suspected mantle-derived (excess) ^{40}Ar .

Figure 3. New ^{40}Ar - ^{39}Ar plateaus generated for Hutaymah samples (see attached file).

Geochemistry

Major, trace, and normalized rare earth element concentrations from 10 samples have been reported in **Table 3** and **Table 4**, respectively (for supplementary geochemical data from Thornber (1992) see appendix). A total alkalis vs. silica diagram comparing the different harrats and Red Sea lavas (**Figure 4**) demonstrates that these new data agree well with those previously reported by Thornber (1992). Hutaymah lavas demonstrate minimal compositional variation, ranging from basanite, to trachy-basalt, to alkaline basalts (44 to 49 wt% SiO₂ and 3.6 to 6.4 wt% Na₂O+K₂O). This limited compositional range is similar to Harrat Lunayyir lavas, but Harrat Rahat lavas express greater variation and more evolved compositions, and generally, the Red Sea lavas are less alkaline.

Samples	HH-1	HH-3	HH-4	HH-6	HH-9	HH-10	HH-11	HH-12	176701	176734
Latitude (N)	26 58 52	26 50 37	26 56 5	26 57 37	27 06 20	27 04 46	27 04 02	27 02 45	27 7 43	27 4 3
Longitude (E)	42 14 24	42 15 1	42 19 17	42 19 29	42 25 17	42 21 39	42 15 52	42 25 30	42 22 18	42 20 57
SiO	46.26	45.51	47.36	45.82	47.75	45.96	48.94	45.60	46.08	46.08
TiO ₂	2.82	2.28	2.71	2.89	1.72	2.62	2.00	2.60	2.34	2.58
Al ₂ O ₃	15.58	14.88	15.46	15.59	15.00	15.29	15.84	14.88	13.95	15.04
FeO	12.30	11.38	10.71	11.24	11.05	11.43	11.69	12.19	11.39	10.87
MnO	0.20	0.18	0.17	0.18	0.17	0.19	0.19	0.20	0.17	0.14
MgO	7.13	10.53	7.37	7.77	10.18	8.87	6.99	8.22	10.28	9.33
CaO	8.93	9.91	9.61	9.92	10.02	11.06	9.81	10.69	10.04	10.08
Na ₂ O	4.61	3.65	4.28	4.29	3.25	2.79	3.56	3.77	3.31	4.42
K ₂ O	1.57	1.18	1.84	1.73	0.64	1.31	0.69	1.32	1.22	1.58
P ₂ O ₅	0.60	0.49	0.50	0.57	0.23	0.48	0.28	0.53	0.37	0.52
Σ	100.00	100.00	100.00	100.00	100.00	100.00	100.00	100.00	99.15	100.64
Mg#	53.73	64.95	57.96	58.06	64.86	60.84	54.49	57.47	64.38	63.22
Ni	116.95	345.85	185.41	198.39	265.36	226.76	172.68	180.19	164.00	214.00
Cr	333.97	463.56	262.94	275.80	701.00	508.19	329.15	556.71		
Sc	31.14	35.49	28.99	28.38	35.95	33.90	38.81	36.81		
V	294.96	351.47	293.20	327.18	321.38	356.60	337.48	346.30		
Ba	394.35	421.97	606.26	589.62	219.52	424.16	542.28	385.97	295.00	417.00
Rb	25.92	22.91	29.09	29.86	10.32	21.22	9.08	23.73		
Sr	937.69	849.04	1068.72	1110.94	540.78	1132.35	543.76	1196.68	644.00	849.00
Zr	304.74	258.21	309.74	306.90	149.29	256.52	160.88	301.90	167.00	181.00
Y ₂	30.73	27.37	26.54	25.53	22.45	28.70	31.75	28.45	24.73	23.91
Nb	119.31	103.13	118.02	124.31	41.76	109.58	38.77	125.03	71.00	84.00
Ga	26.08	25.36	26.88	29.84	25.36	25.81	28.50	25.54		
Cu	63.59	106.90	79.86	85.62	102.43	74.61	122.55	72.73	70.00	80.00
Zn	112.47	114.30	107.46	108.47	113.68	102.70	133.14	120.11	126.00	151.00
Pb	2.48	2.03	3.77	2.48	0.96	2.37	1.94	2.05	2.00	
La	42.45	51.36	57.70	58.87	17.93	40.11	15.83	40.46		
Ce	85.56	86.06	100.68	99.08	38.69	83.34	45.36	90.47	71.00	86.00
Th	4.97	7.34	7.94	10.04	2.96	6.84	3.42	4.86		
Nd	39.07	32.31	38.26	36.39	20.85	34.64	21.46	38.37		
U	1.65	2.40	3.96	2.86	1.09	1.76	0.00	2.53		

Table 3. Whole rock major and trace element concentrations from select Harrat Hutaymah lavas. Data obtained using XRF and ICP-MS. Major element concentrations expressed as weight percent oxides. Trace element concentrations are expressed as ppm. Iron is reported as total iron (II) oxide (FeO*).

Samples	HH-1	HH-3	HH-4	HH-6	HH-9	HH-10	HH-11	HH-12	176701	176734
Normalized REE										
La	151.73	169.63	200.93	207.06	65.32	150.90	72.68	152.83	144.34	199.75
Ce	119.73	115.57	134.24	137.28	49.72	110.60	54.65	119.62	110.19	141.34
Pr	95.58	84.67	97.75	99.90	40.22	86.55	45.84	94.82	86.51	105.89
Nd	77.55	64.33	74.07	75.78	34.23	68.16	40.16	75.52	69.57	81.87
Sm	49.85	39.57	45.35	45.60	25.97	43.45	32.05	47.30	46.00	50.25
Eu	44.08	35.95	38.15	40.35	24.46	38.71	30.03	42.61	39.62	42.35
Gd	32.74	26.61	28.80	29.77	19.63	29.24	24.56	31.43	30.80	32.09
Tb	27.37	22.19	22.78	23.75	17.27	23.94	21.87	25.86	26.33	26.39
Dy	22.16	18.42	18.51	19.28	15.02	20.02	19.56	20.89	21.64	21.41
Ho	18.58	15.59	15.47	15.65	12.87	16.52	17.35	17.53	18.41	17.85
Er	15.68	13.07	12.94	12.97	11.23	13.75	15.30	14.73	15.72	14.77
Tm	13.94	11.54	11.34	11.19	9.76	11.82	13.67	12.81	14.25	13.18
Yb	12.37	10.52	10.34	10.12	8.92	11.05	12.20	11.40	12.48	11.79
Lu	11.43	10.07	9.97	9.70	8.88	10.97	12.41	10.91	12.29	11.83
Nb/Zr	0.39	0.40	0.38	0.41	0.28	0.43	0.24	0.41	0.43	0.46
(La/Yb) _n	12.27	16.13	19.43	20.46	7.32	13.65	5.96	13.41	11.56	16.94
(Dy/Yb) _n	1.79	1.75	1.79	1.91	1.68	1.81	1.60	1.83	1.73	1.82
Ce/Y	2.78	3.14	3.79	3.88	1.72	2.90	1.43	3.18	2.87	3.60
(La/Sm) _n	3.04	4.29	4.43	4.54	2.52	3.47	2.27	3.23	3.14	3.97
(Sm/Yb) _n	4.03	3.76	4.39	4.51	2.91	3.93	2.63	4.15	3.68	4.26
(Zr/Y) _n	4.02	3.83	4.73	4.88	2.70	3.63	2.06	4.31	2.74	3.07

Table 4. Rare earth element concentrations normalized to C1 Chondrite. Normalization values from McDonough & Sun (1989). Data reported in ppm.

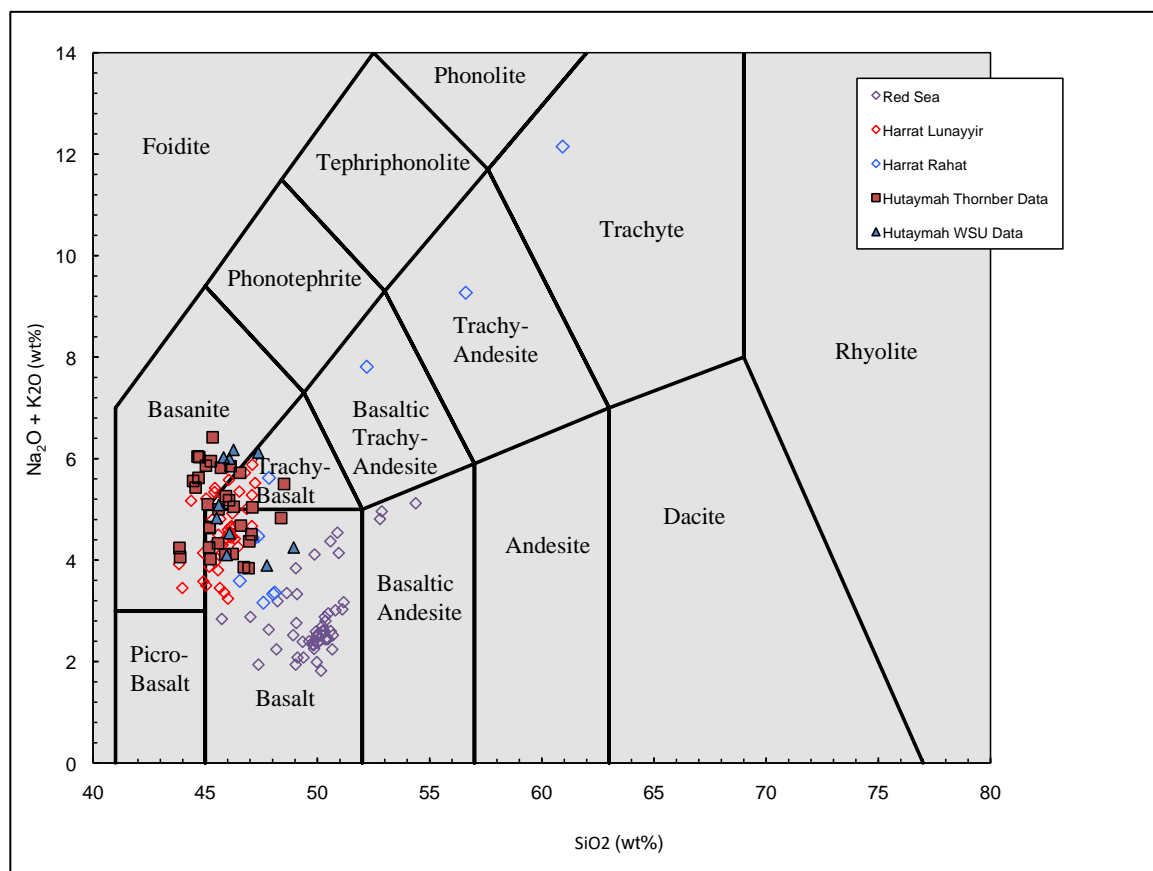


Figure 4. Total Alkalis vs. Silica diagram comparing harrat province fields and Red Sea lavas. Harrat Hutaymah lavas are red squares (Thornber, 1992) and blue triangles (this study), Harrat Lunayyir are orange diamonds (Duncan and Al-Amri, 2013), Harrat Rahat are green diamonds (Moufti et al., 2005), and Red Sea lavas are purple diamonds (Kelley et al. 2013, and Vlastelic et al., 1998).

DISCUSSION

Timing of Hutaymah Magmatism

The age of Harrat Hutaymah has been estimated twice previously, employing the K/Ar dating technique in both occasions. These studies have yielded ages of 0.1 to 2.65 Ma (Thornber, 1992), and 1.84 ± 0.05 Ma (Pallister, 1984), respectively. While the new ^{40}Ar - ^{39}Ar ages reported here fall within this range, these new data suggest that Hutaymah volcanism occurred over a much shorter time period from 500-852 ka. Most importantly, sample HH-1 was collected at the same location, *Al Hutaymah* crater (see **Figure 2**), from which Pallister (1984) attained an age of 1.84 ± 0.05 Ma, but reports a significantly younger age of 580 ± 94 ka (**Table 2**). The disparity between previous K/Ar and new ^{40}Ar - ^{39}Ar ages can be explained by the abundant xenolithic material commonly found in Hutaymah lavas.

Field observation and petrographic analysis of Hutaymah rocks reveal that they contain an abundance of xenolithic material. This abundant foreign material has been interpreted as the cause of undeveloped ^{40}Ar - ^{39}Ar plateaus for sample HH-3 and HH-4 (**Table 2** and **Figure 3**), and is likely responsible for the wide range of previously reported K/Ar ages. Sample HH-4 reports an age of 2.15 ± 0.88 Ma, which falls within the range of reported K/Ar ages, however, the failure to produce a defined plateau age is a clear indication that the dating process failed. The new ages reported here are more robust than previous ages as the presence of xenolithic material can be identified upon the

failure of a sample to produce a meaningful plateau.

Magmatic Evolution

Variation diagrams for select major elements are shown in **Figure 5**. SiO₂, CaO, and FeO* remain constant from 14 to 5 wt% MgO, while TiO₂, NaO, and Al₂O₃ generally increase linearly. These trends are consistent with olivine fractionation over the entire range of MgO contents. TiO₂ and CaO show the greatest scatter among the major elements. Although there is no definitive change in slope observed in the data, it is possible that the scatter is the result of late stage introduction of CPX (titan-augite) as a crystallizing phase. The conclusion that the system is dominantly controlled by olivine is supported by petrographic analysis, as the majority of olivine observed in thin section is euhedral. Minor euhedral CPX is also present in thin section, supporting the possibility of CPX being introduced as a major fractionating phase late in the evolution of the magma. There is no evidence for plagioclase fractionation. The most primitive Hutaymah samples, based on highest MgO content and Mg#, contain greater than 14 wt% MgO. These samples are suspected of undergoing slight olivine accumulation, as more reasonable primitive MgO contents are around 12-13%. Clearly sieved olivine observed in petrographic analysis support this hypothesis, but mineral compositions are required to be certain.

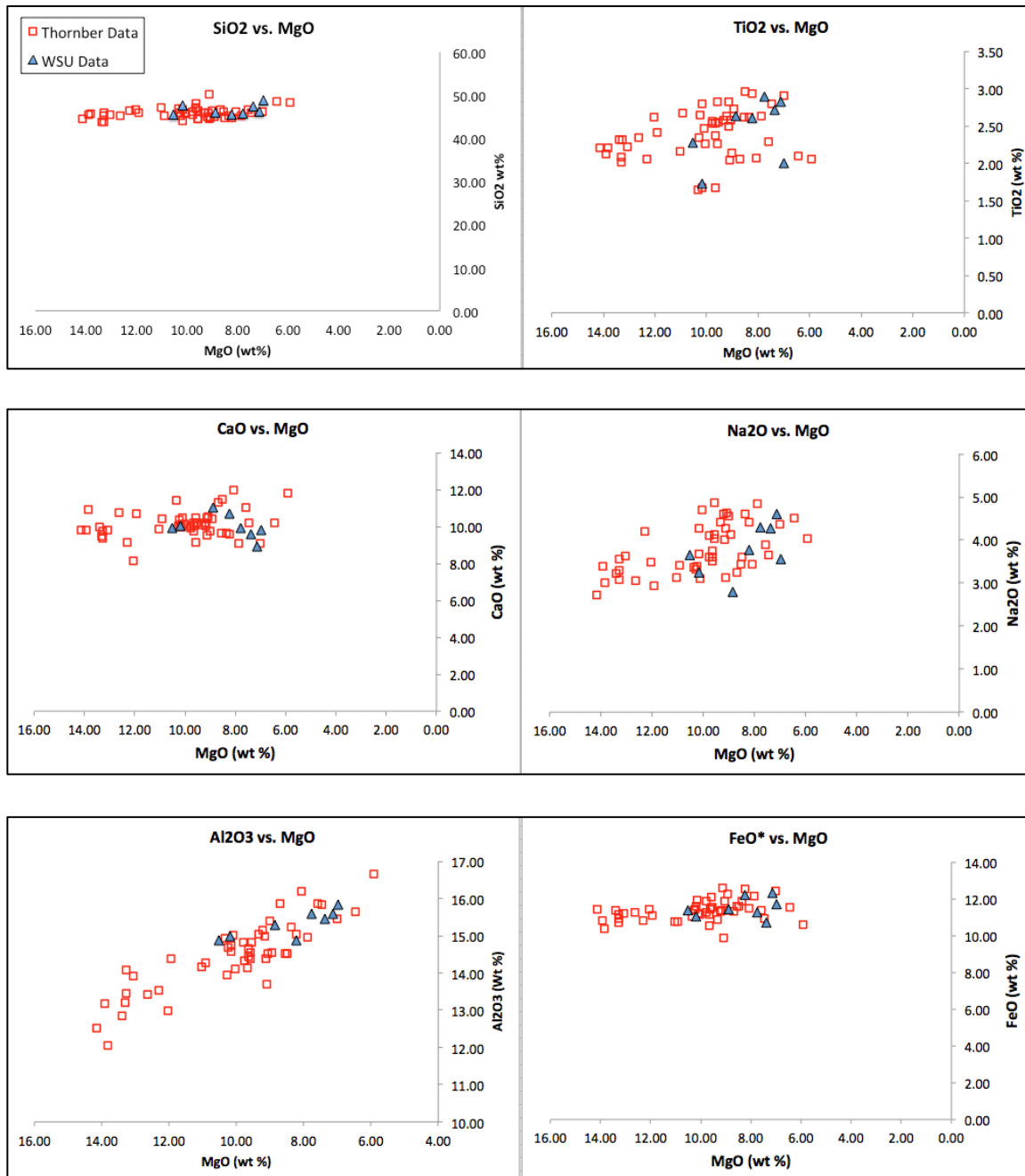


Figure 5. Major element variation diagrams for Harrat Hutaymah samples.

Crystallization trends produced by MELTS were compared to trends on major element variation diagrams. **Figure 6** shows the liquid line of descent calculated by the MELTS model, using the initial composition found in **Table 5**, compared to major element variation diagrams for Al_2O_3 , FeO^* , and CaO plotted against MgO . These four elements were selected because they are the most abundant constituents found in the mineral phases (olivine, plagioclase, and pyroxene) identified in Hutaymah rocks, and thus provide a good approximation of the models validity. The starting composition for this model was selected in an attempt to model the most primitive sample that has not undergone olivine accumulation. The crystallization trends predicted by this model correspond well with the element variation diagrams.

Oxide	Wt.%
SiO_2	45.1
TiO_2	2.3
Al_2O_3	13.4
Fe_2O_3	0.0
Cr_2O_3	0.0
FeO	11.2
MnO	0.1
MgO	12.6
NiO	0.0
CoO	0.0
CaO	10.7
Na_2O	3.1
K_2O	1.0
P_2O_5	0.5
H_2O	0.0
Total	100.0

Table 5. Starting composition used for MELTS modeling expressed as wt% of oxides. In models where total wt% oxides exceeded 100% concentrations were renormalized to 100%. Total iron is expressed as FeO^* .

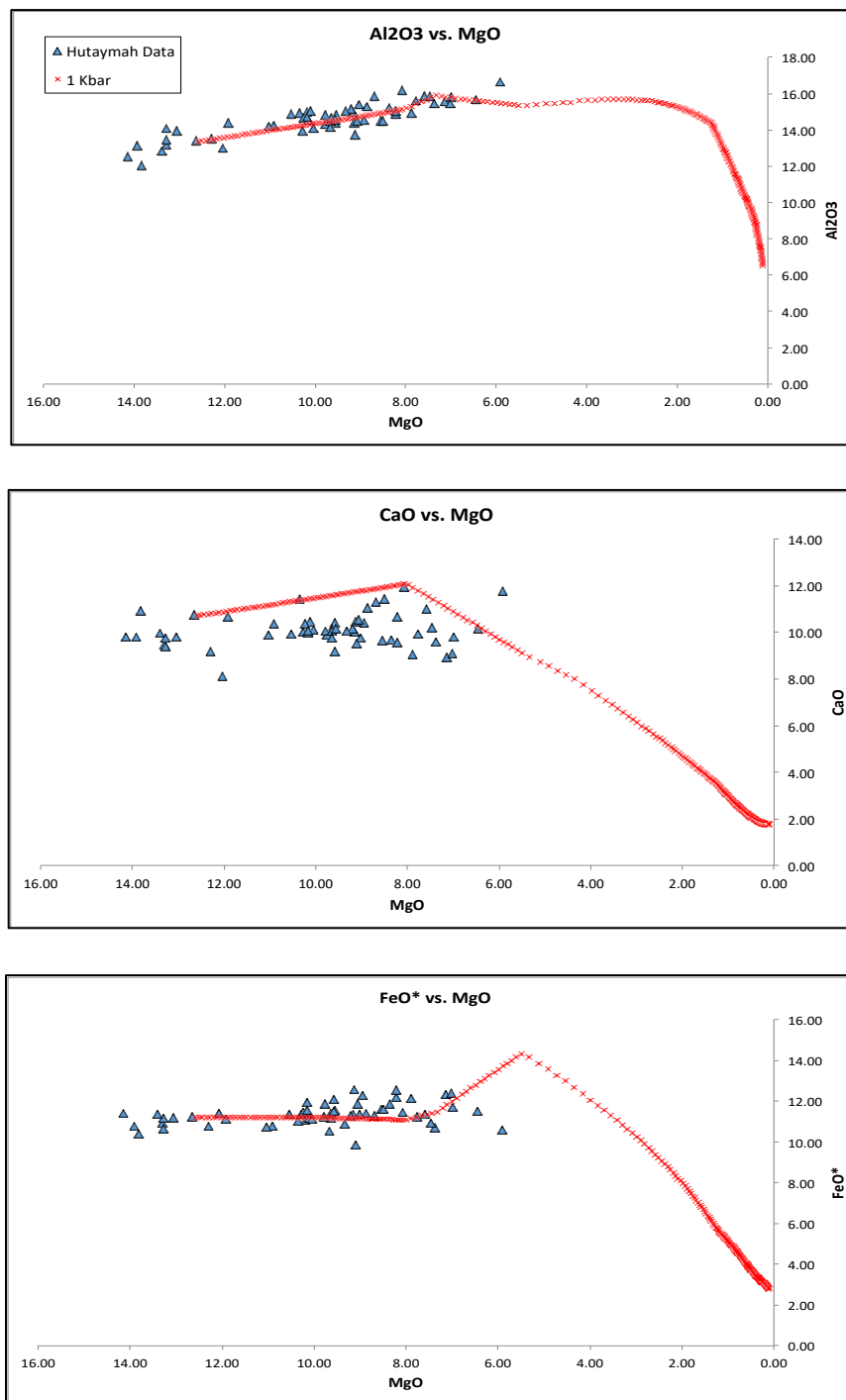


Figure 6. Liquid lines of descent modeled by MELTS at 1 kbar with oxygen fugacity

constrained at the QFM redox buffer. Starting composition found in **Table 5**.

The same starting composition was used to model crystallization trends under variable pressure, water content, oxygen fugacity (fO_2), and initial CaO and TiO_2 content, in order to constrain the conditions under which Hutaymah magmas formed. **Figure 7** shows variations in liquid lines of descent predicted by models with variable pressures. Fractionation trends were modeled at 1, 5, and 10 kbars. Fractionation trends predicted by the model at both 1 and 5 kbars fit the data well, whereas trends produced by the model at 10 kbars do not adequately follow the data trends. For both Al_2O_3 and FeO^* changes in pressure do not considerably effect the model trend until pressure exceeds 5 kbars. The fractionation trend for CaO is the most sensitive to changes in pressure, likely due to changing the stability of CPX, with the inflection point shifting to higher MgO contents with higher pressure. Despite the stronger influence of pressure on CaO trends, the best fit is still 5 kbars, with the inflection point at 10 kbars occurring far too early in the system (~11wt% MgO). Due to the strong control of olivine on the system, with limited influence of other phases on the crystallization trends, it is difficult to further constrain the pressure at which crystallization occurred. Therefore, with the best fit for all three variation diagrams ranging from 1 to 5 kbars, it is suggested that crystallization is restricted to mid to shallow crust depths ranging from 3 to ~15 km.

Variations in liquid lines of descent predicted by models with variable water content are shown in **Figure 8** and **Figure 9**. Initially models were run at 1 kbar, but this limited the possible water contents to below 2.0 wt%, likely because water becomes significantly less soluble at lower pressures. In order to model a larger range of water contents the model was also run at a pressure of 5 kbars. This change allowed models to

reach up to 5.0 wt% water while satisfying the pressure constraints discussed above. At both 1 and 5 kbars trends produced by 0.1 and 2.0 wt% water bracket the data, with 1.0 wt% H₂O providing the best fit. This result is reasonable as 1.0 wt% H₂O is consistent with other plume generated basalts. **Figure 8** demonstrated the crystallization trends produced at 1 kbars and **Figure 9** demonstrated the crystallization trends at 5 kbars. **Figure 10** shows variations in liquid lines of descent predicted by models using different redox buffers to constrain oxygen fugacity (f_{O_2}). Crystallization trend for both CaO and FeO* diagrams show significant variation with differing f_{O_2} conditions. The trend produced by the QFM (quartz-fayalite-magnetite) redox buffer most closely approximates the trends on the variation diagrams, and thus, likely describes the f_{O_2} conditions under which Hutaymah rocks crystallized.

Both CaO and TiO₂ variation diagrams show the least developed crystallization trends for Hutaymah rocks. **Figure 11** and **Figure 12** show crystallization trends produced by models with varying initial CaO and TiO₂ concentrations, respectively. **Figure 11** demonstrates that the range of CaO concentrations seen in Hutaymah rocks can be accounted for with initial CaO contents ranging from 9.25 wt% to 10.75 wt%, while **Figure 12** demonstrated that the range of TiO₂ concentrations can be modeled with initial TiO₂ ranging from 1.6 wt% to 2.34 wt%. These variations suggest that the magmas from which Hutaymah rocks crystallized were likely variable in their initial CaO and TiO₂ concentrations.

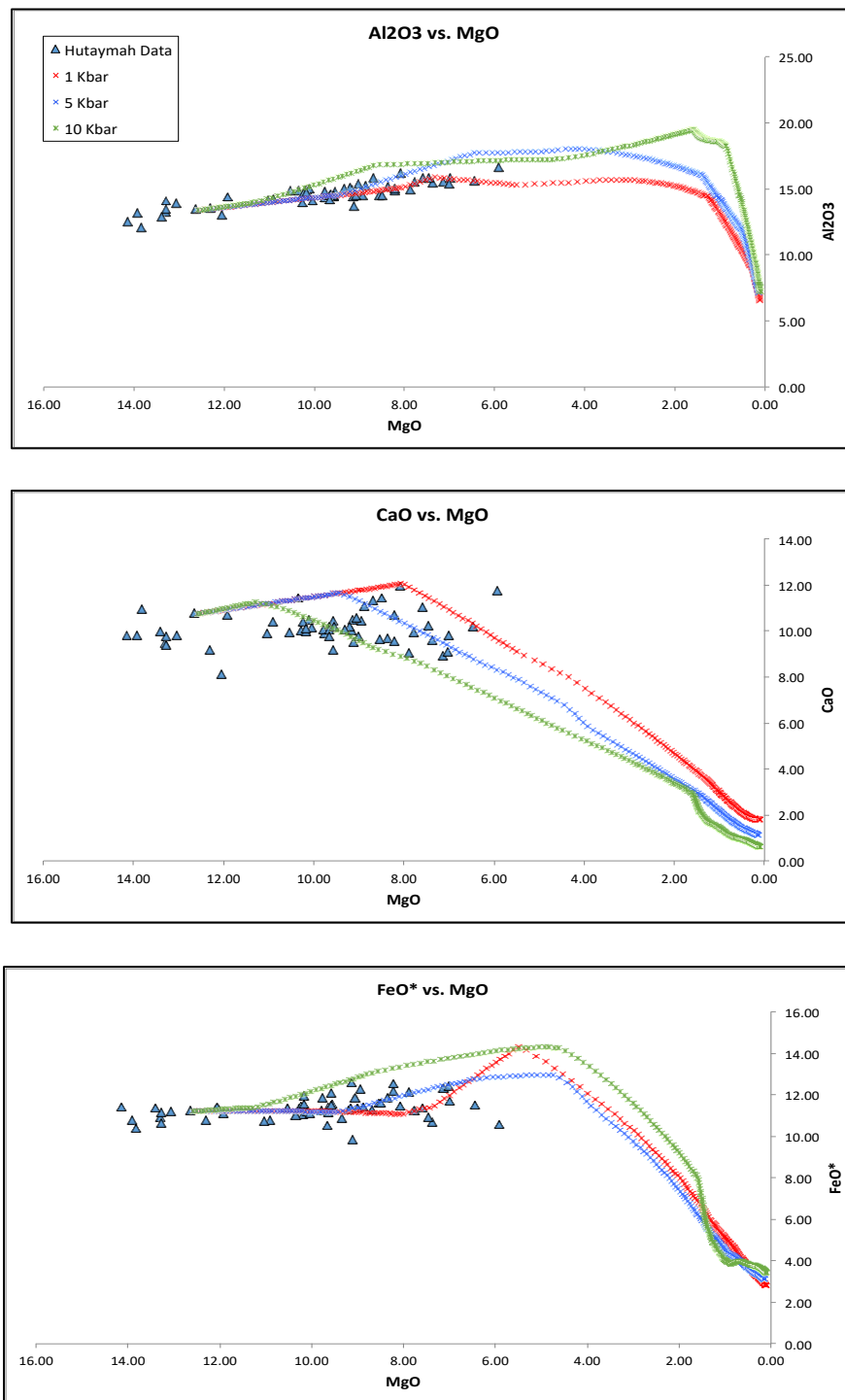


Figure 7. Liquid lines of descent modeled by MELTS at variable pressures with oxygen fugacity constrained at the QFM redox buffer. Starting composition found in **Table 5**.

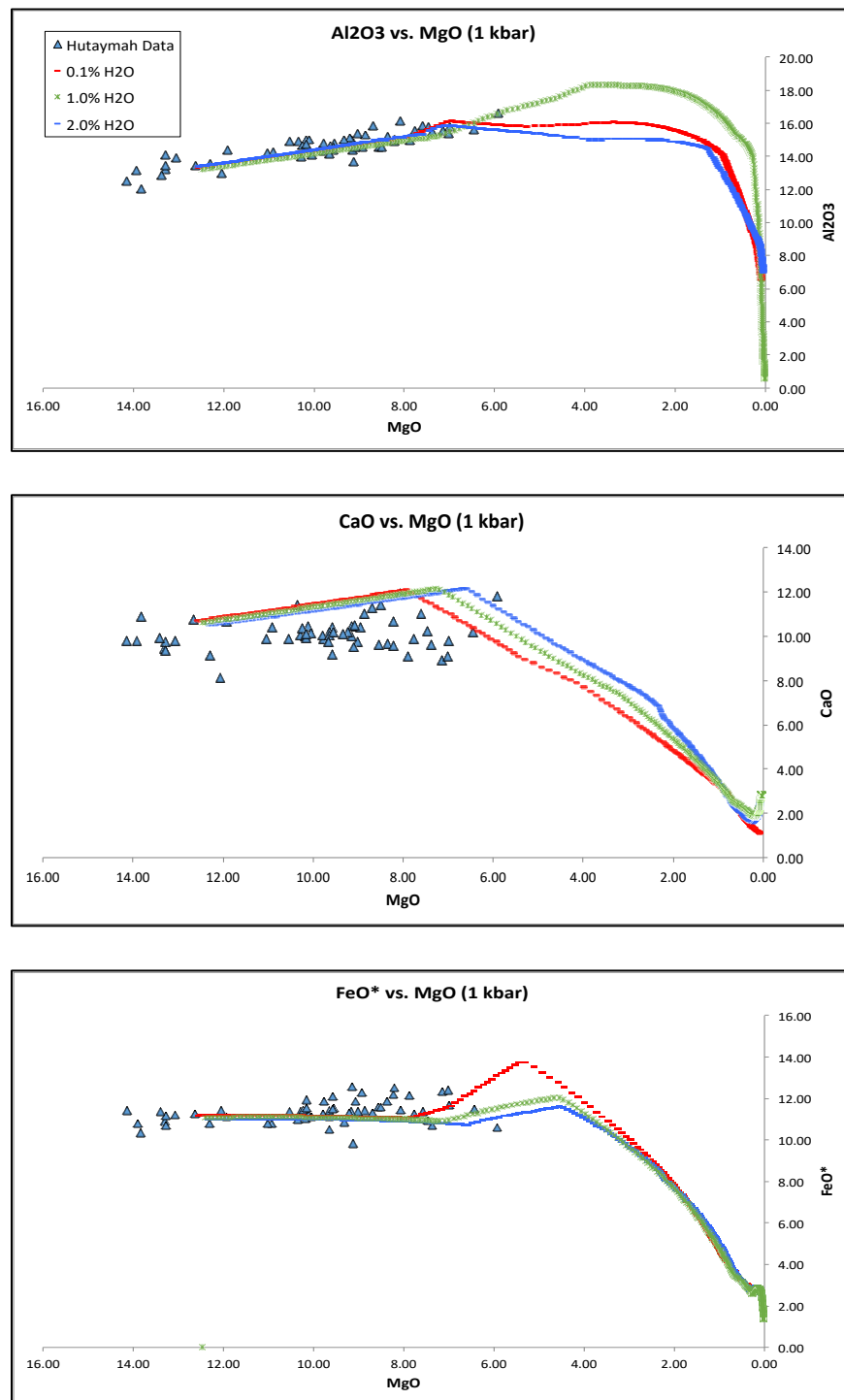


Figure 8. Liquid lines of descent modeled by MELTS at variable water content at 1 kbar with oxygen fugacity constrained at the QFM redox buffer. Starting composition found in

Table 5. For water content greater the 0.1 wt% major oxide concentrations were renormalized to 100%.

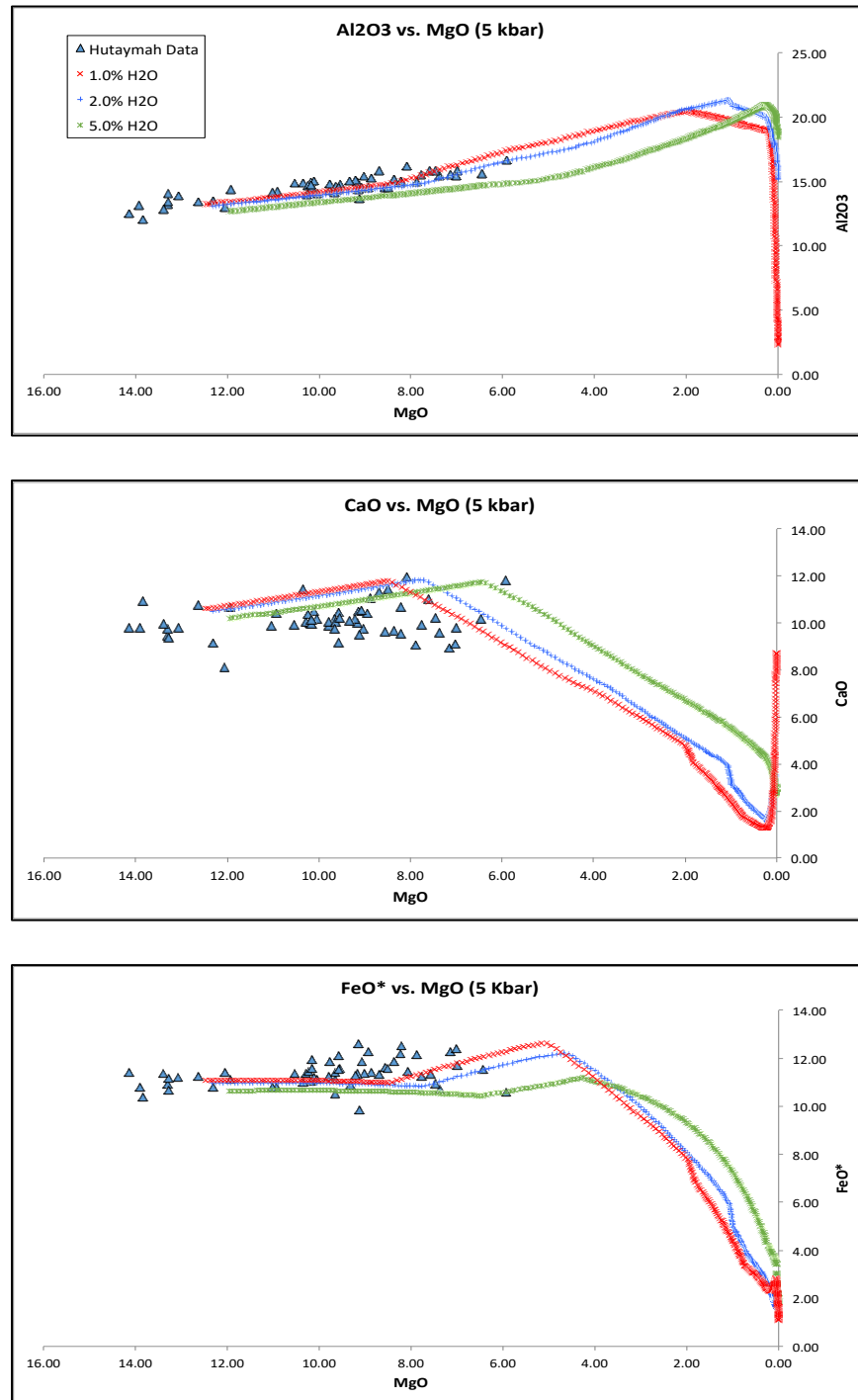


Figure 9. Liquid lines of descent modeled by MELTS at variable water content at 5 kbar with oxygen fugacity constrained at the QFM redox buffer. Starting composition found in **Table 5**. For water content greater the 0.1 wt% major oxide concentrations were

renormalized to 100%.

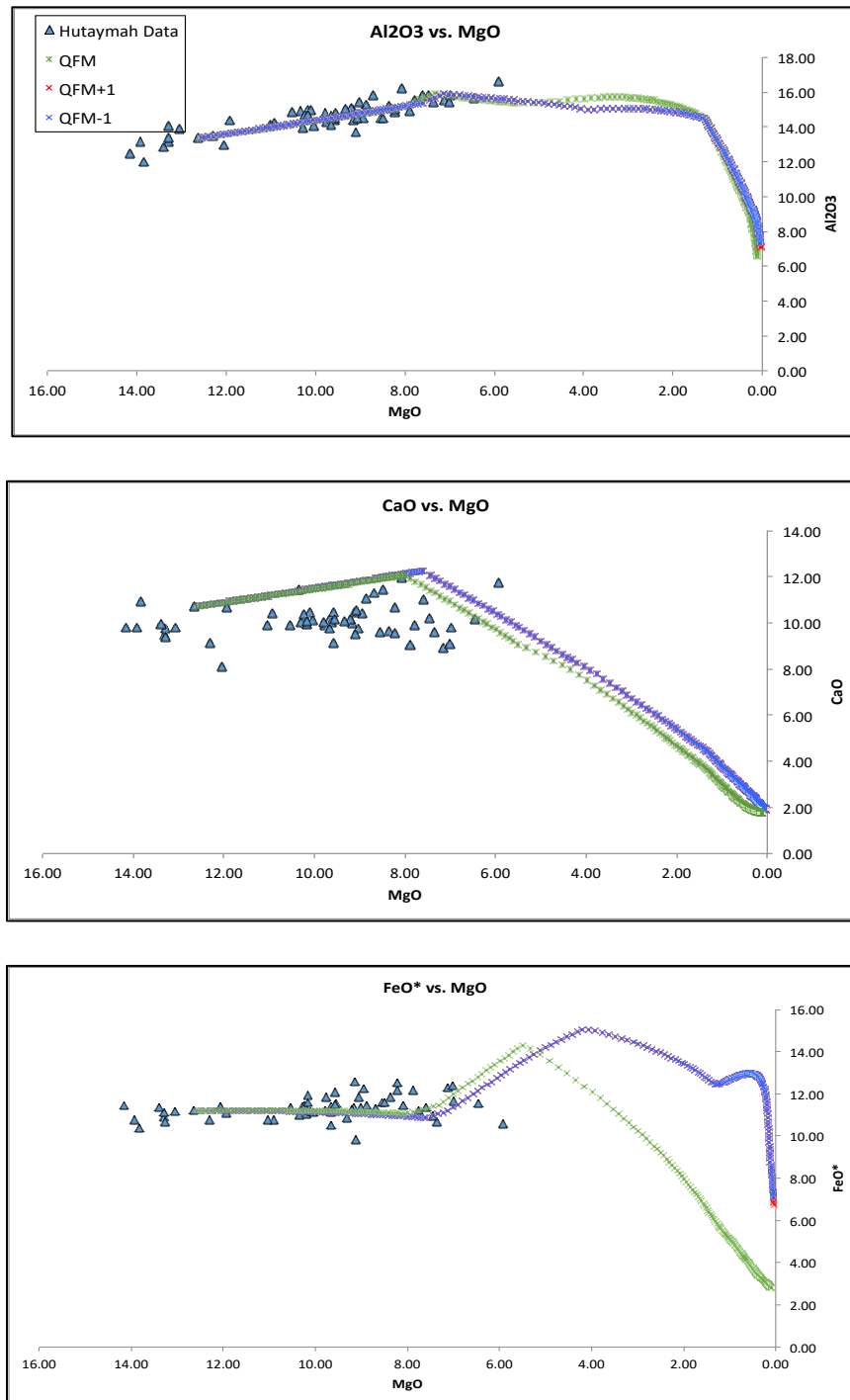


Figure 10. Liquid lines of descent modeled by MELTS using various redox buffers at 1 kbar. Starting composition found in **Table 5**.

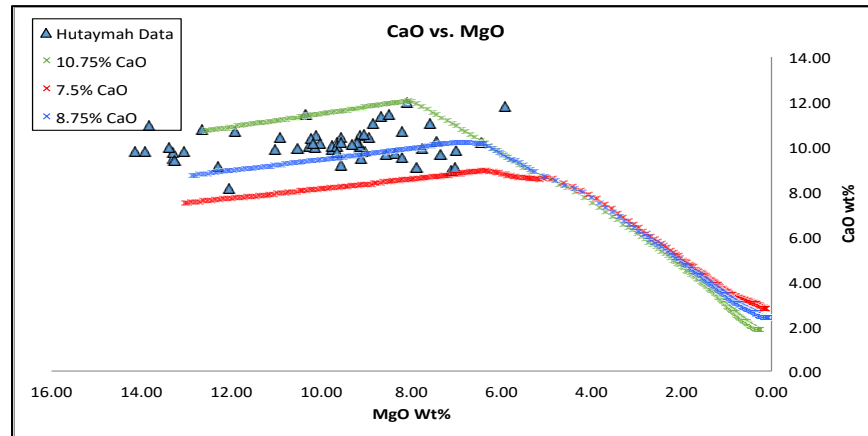


Figure 11. Liquid lines of descent modeled by MELTS using various initial CaO concentrations at 1 kbar with oxygen fugacity constrained at the QFM redox buffer. Starting composition found in **Table 5**. Major oxide concentrations were renormalized to 100%.

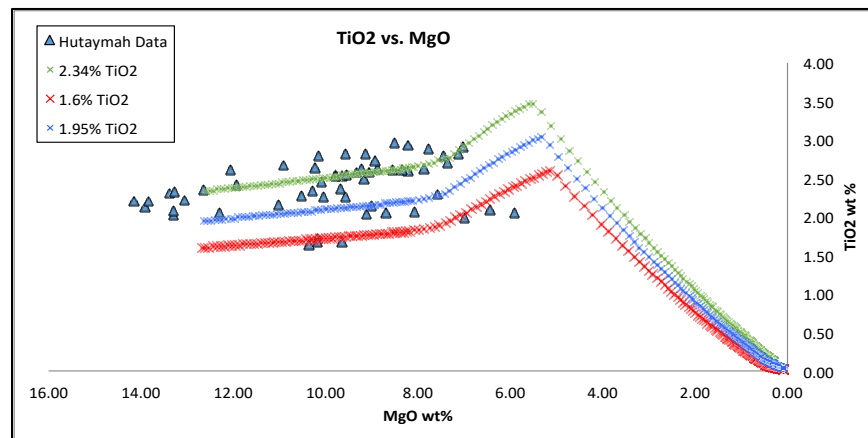


Figure 12. Liquid lines of descent modeled by MELTS using various initial TiO₂ concentrations at 1 kbar with oxygen fugacity constrained at the QFM redox buffer. Starting composition found in **Table 5**. Major oxide concentrations were renormalized to 100%.

Constraints on Mantle Source Composition and Melting

Variations in REEs and trace elements can be used to constrain the mantle source composition and melting conditions involved in magma generation. **Figure 13** shows chondrite normalized REE patterns for Hutaymah rocks. As demonstrated in **Figure 13** REE patterns for Harrat Hutaymah rocks are strongly enriched in light rare earth elements (LREEs) and relatively depleted in heavy rare earth elements (HREEs). This pattern is commonly produced by partial melting of a garnet bearing mantle source. The HREEs prefer to partition into the garnet phase if present, as a result, during low degrees of partial melting garnet will prevent HREEs from entering the melt causing the characteristic REE patterns seen in Hutaymah rocks. If garnet is present in the mantle source then Hutaymah magmas have to originate in the garnet stability zone, at depths greater than ~60 km.

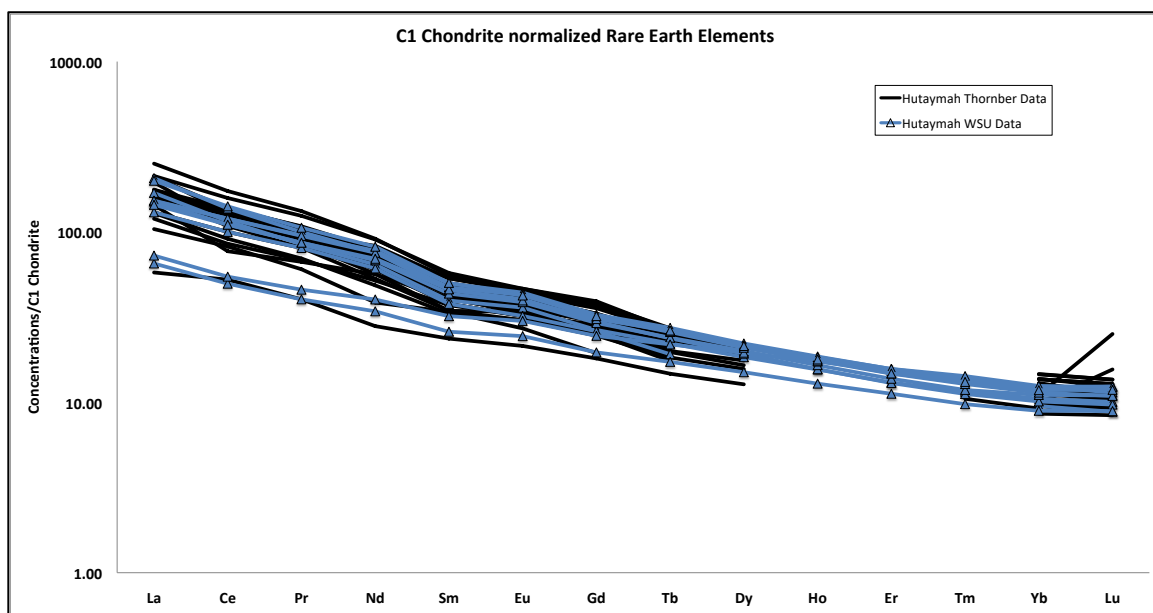


Figure 13. REE diagram for Harrat Hutaymah samples. REE concentrations are normalized to C1 chondrite using concentrations from McDonough & Sun (1989).

In order to test the validity of this hypothesis and further constrain the source composition and degree of partial melting a batch-melting model was developed. The source compositions given for primitive and depleted garnet spinel lherzolite and spinel lherzolite by Gurenko and Chaussidon (1995) serve as the basis for this model. In order to bracket the REE concentrations in **Figure 13**, the model was run for variable source garnet concentrations (between 0% and 15%). Also, a $(La/Sm)_n$ vs. $(Sm/Yb)_n$ plot was constructed comparing Hutaymah data and batch melting results with variable concentrations of source garnet (**Figure 14**), as these ratios are highly sensitive to the presence of garnet in the system. Based on the model results, the range of Hutaymah REE concentrations can be accounted for by 0.5 to 8% batch melting of a primitive mantle source containing 4 to 15% garnet. As seen in **Figure 14**, 15% garnet still falls short of capturing the entire range of Hutaymah data. Increasing the source composition to 20% garnet can model the more extreme Hutaymah data, however this amount of garnet pushes the boundary of reasonable mantle compositions. Although, it is possible that these extreme Hutaymah values are the result of melting locally more garnet rich mantle (~20%), it is also a possibility that the initial $(Sm/Yb)_n$ ratio of the mantle is higher than that reported in Gurenko and Chaussidon (1995), which would shift the modeled trends to the right, accounting for the full range of Hutaymah data. Batch melting of a garnet free source failed to adequately account for the depletion of HREEs seen in the Hutaymah REE pattern. Although the batch-melting model was able to bracket the REE variability, it proved difficult to accurately match the slope the REE pattern.

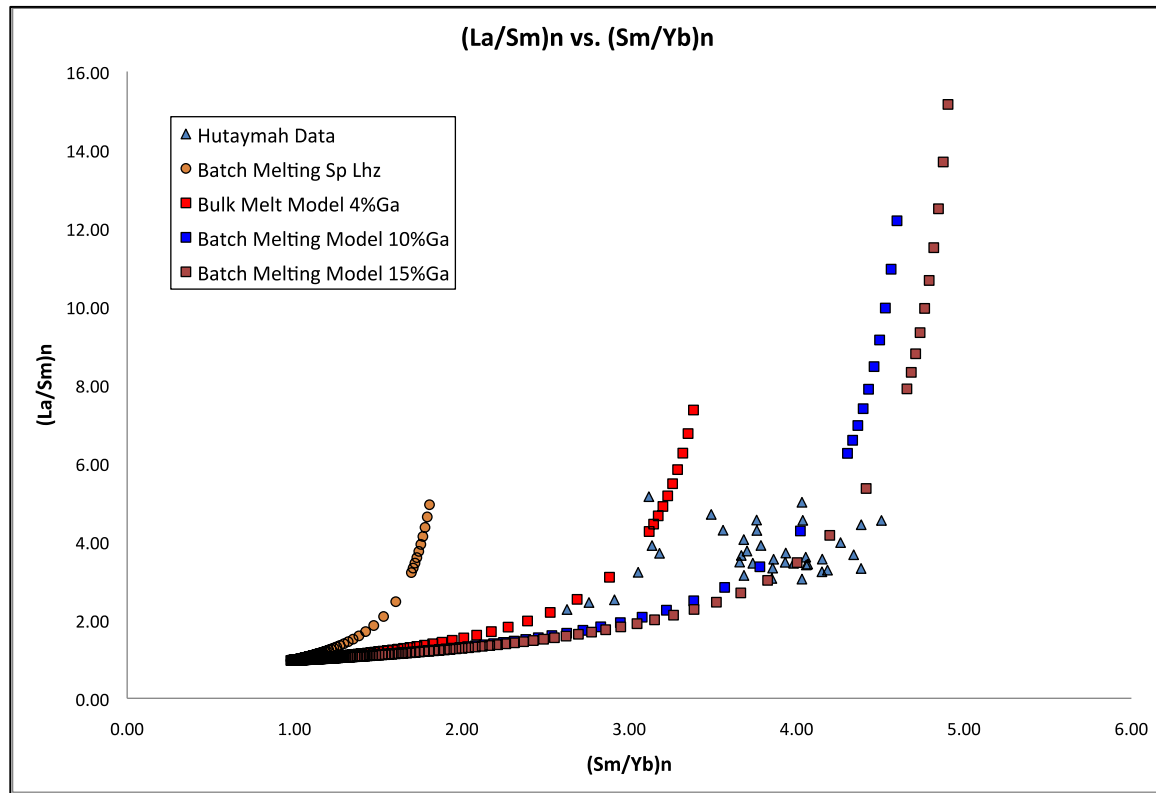


Figure 14. $(La/Sm)_n$ vs. $(Sm/Yb)_n$ plot for Harrat Hutaymah data (blue triangles), and melting of various source compositions (orange circles, spinel lherzolite; red squares, 4% garnet; blue squares, 10% garnet; and brown squares, 15% garnet).

In order to more accurately bracket the concentration of garnet in the mantle source and the degree of melting a fractional crystallization model was developed. The results of this can be seen in **Figure 15**. As demonstrated in **Figure 15**, the upper bound of Harrat Hutaymah's REE diagram is best modeled by melting of a mantle source containing 4% garnet with 21% fractional crystallization. The lower bound is best modeled by melting a source containing 10% garnet with 34% fractional crystallization. Therefore, Hutaymah REE patterns are best reproduced by low degrees of partial melting (0.5% to 8%) of a primitive mantle source containing 4% to 10%, possibly more locally, garnet, that then undergoes 21% to 34% fractional crystallization.

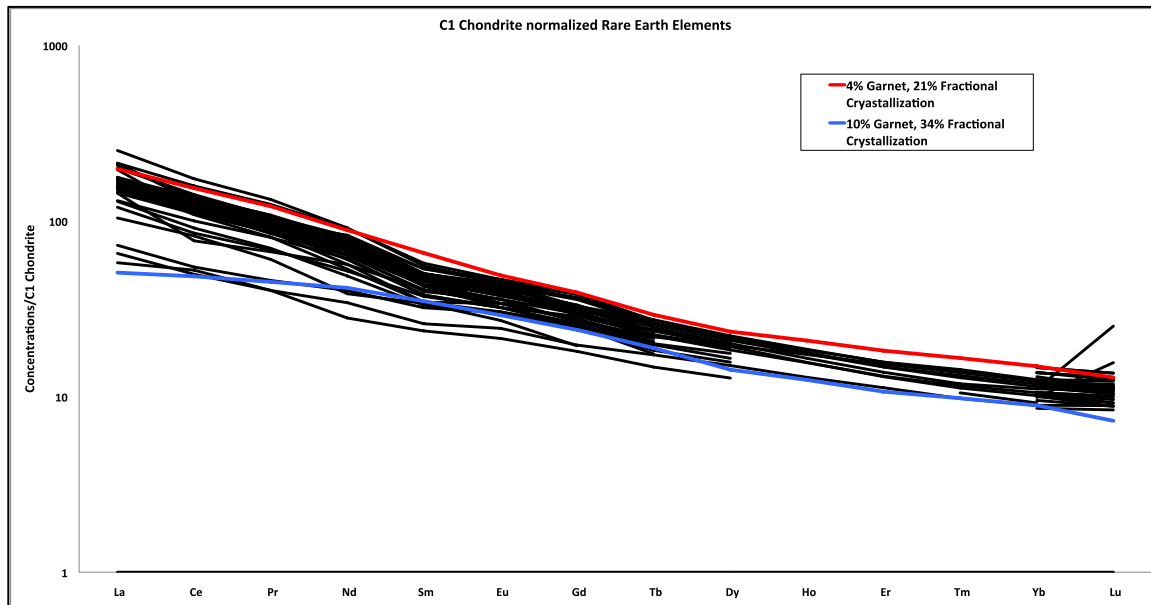


Figure 15. Fractional crystallization model results. The range of Harrat Hutaymah REE concentrations can be best approximated by of a melting mantle source containing 4-10% garnet with 21-34% fractional crystallization. Model uses primitive mantle source compositions from Gurenko and Chaussidon (1995) (**Table 1**).

Evidence for Mantle Plume Influence

To determine whether a mantle plume has influenced Harrat Hutaymah rocks, their compositions have been plotted against the Icelandic Array of Fitton et al. (1997), along with samples from Harrat Lunayyir, Harrat Rahat, and the Red Sea (**Figure 16**). The fact that the majority of samples plot within the Icelandic Array is evidence that their trace element chemistry is not inconsistent with a plume-related source. It is also important to note that $^3\text{He}/^4\text{He}$ ratios measured at Harrat Rahat range from 9.3 to 11.7 Ra, further supporting the idea that these rocks have been influenced by a plume source (Murcia et al., 2013).

The mantle plume hypothesis is also supported by geophysical data. As reported by Chang and Van der Lee (2011), a distinct low-velocity anomaly has been identified beneath the Afar region. These anomalies have been attributed to horizontal asthenospheric flow, along thin lithospheric channels, radially away from the Afar plume. Two such channels have been identified. One is located east of Afar, following the Gulf of Aden, while the other extends northward beneath the southern Red Sea, but rather than extending to the central Red Sea, it continues northwards beneath western Arabia (Chang and Van der Lee, 2011). The low-velocity anomaly below the Harrat Hutaymah, sourced from the Afar region, supports the idea the widespread volcanism in western Arabia is influenced by northward flow from the Afar plume.

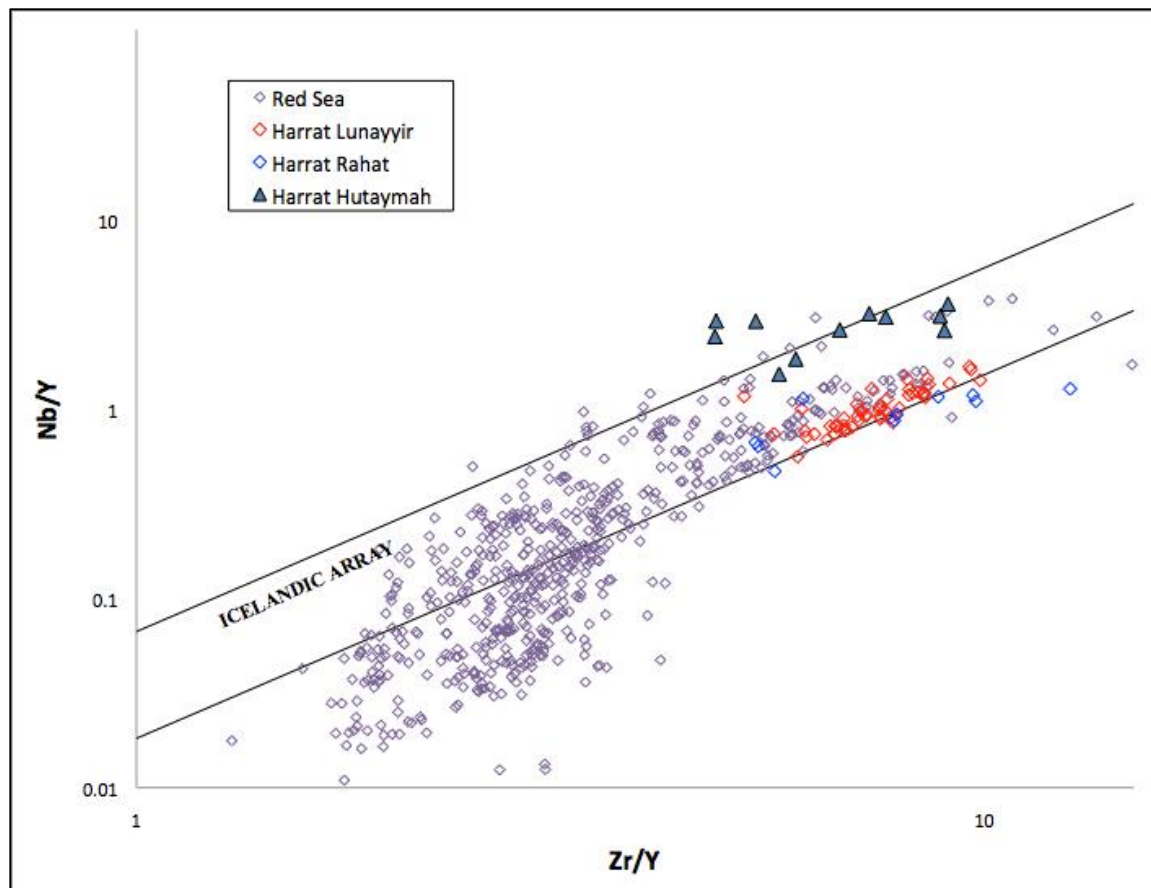


Figure 16. Nb/Y vs. Zr/Y plot for Harrats Hutaymah, Rahat, Lunayyir, and Red Sea samples. The majority of samples plot within the Icelandic Array of Fitton et al. (1997), suggesting they are influenced by a plume-related source.

Harrat Hutaymah Petrogenesis and Regional Implications

The data obtained over the course of this research challenges previous models for the petrogenesis of Harrat Hutaymah and the Harrat Region as a whole. New ^{40}Ar - ^{39}Ar ages ranging from 500 to 852 ka suggest that Harrat Hutaymah formed much more rapidly than previously thought. Also, samples utilized in this research, from Harrat Hutaymah as well as Harrat Lunayyir and Rahat, are consistent with formation from a plume-related source (Fitton et al., 1993). Additionally, batch melting and fractional crystallization models show that it is possible to produce the full range of REE compositions of Harrat Hutaymah rocks through 1 to 8% partial melting of a primitive mantle source containing 4 to 10% garnet, coupled with 21 to 34% fractional crystallization.

It has been proposed that the petrogenesis of Harrat Hutaymah and the entire Harrat Region can be explained by simple decompression melting related to the rifting of the Red Sea (Thorner, 1992). However, the variability of depth and degree of melting, as well as the significant compositional variation observed throughout the Harrat Region, suggest that the situation is more complicated. **Figure 17**, modified from Fram and Leshner, (1993), allows for a comparison of depth and degree of partial melting for multiple Saudi Arabian volcanic fields, providing insight into the structure of the lithosphere/asthenosphere boundary below the Harrat region. The new data reported here agree well with **Figure 17** for Hutaymah rocks, suggesting a depth of melting of 18-24 kbar (~60-75 km) with less than 8% partial melting. For comparison **Figure 17** suggest Harrat Lunayyir magma is generated at 20 to 25 kbar (60-75 km) with 7 to 12% melting, Harrat Rahat magma is generated at 5 to 15 kbar (15-45 km) with 10 to 17% melting, and

Red Sea magma is generated at 0 kbar (essentially no lithosphere) and up to 25% melting. This insight into the shape of the lithosphere/asthenosphere boundary combined with new data from this research allows for a new model to be proposed.

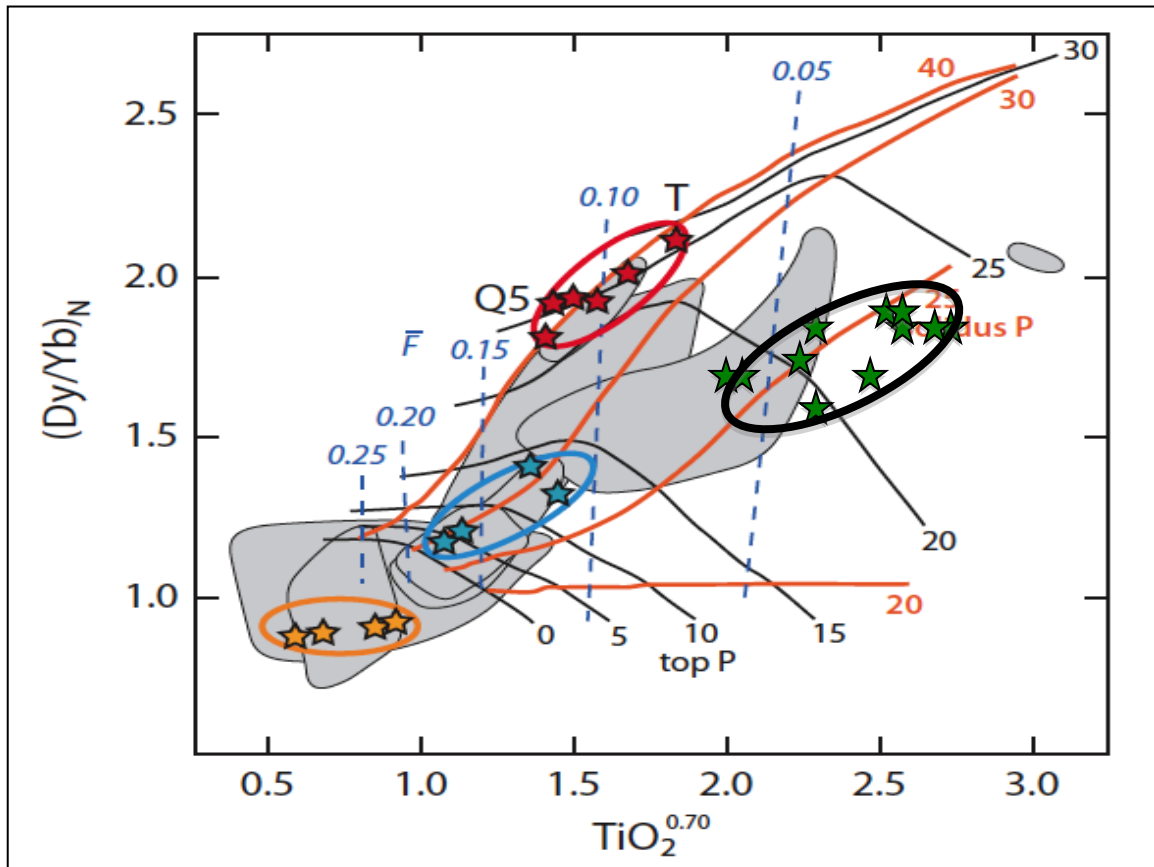


Figure 17. . [Dy/Yb]_N vs. TiO₂^{0.70} plot for multiple Saudi Arabian volcanic fields (after Fram and Leshner, 1993). Heavy curves show depth of onset of melting (solidus, bold orange numbers in kbar), light curves show the top of the melt zone (lithosphere thickness, black numbers in kbar), and dashed vertical lines are degree of melting (blue numbers are fractions). Gray fields are for volcanic formations in Iceland and the NAIP, these are not identified here, but show progressive thinning of north Atlantic lithosphere and a decrease in the depth of mantle melting. For comparison, Harrat Hutaymah compositions (green stars), Harrat Lunayyir compositions (red stars), Red Sea compositions (orange stars), and Harrat Rahat compositions (blue stars).

The model proposed here explains the petrogenesis of Harrat Hutaymah and the rest of the Harrat region with regional extension resulting in decompression melting coupled with northward asthenospheric flow from the Afar plume (**Figure 18**). It is likely that the older, Red Sea parallel, Harrat region volcanism (>12 Ma) is the result of simple decompression melting due to rifting of the Red Sea, as suggested by their orientation and tholeiitic compositions. However, the younger (<12 Ma) N-S oriented volcanic centers (Hutaymah, Lunayyir, Rahat etc.) that together make up the Makkah-Madinah-Nafud (MMN) line are best explained by the model in **Figure 18**. Regional thinning along the N-S trending MMN line resulting in decompression melting, coupled with northward asthenospheric flow of the Afar plume is the best way to explain the variable depth and degree of melting and compositional variation observed across the Harrat Region.

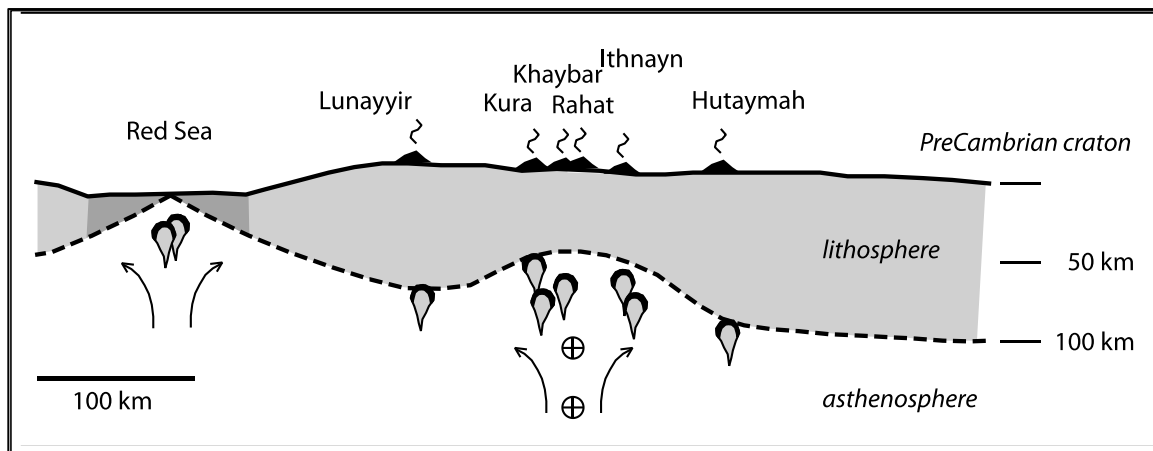


Figure 18. Conceptual model of Harrat Region petrogenesis. Regional thinning along the N-S trending MMN line allows for decompression melting, when coupled with northward asthenospheric flow from the Afar plume this model explains the variable depth and degree of melting and the compositional variation observed throughout the region.

ACKNOWLEDGEMENTS

Kyle Krawl provided assistance with instruction in using the geochemical modeling software. ICP-MS and additional XRF analyses were provided by the Washington State University GeoAnalytical Laboratory. Dr. Dan Miggins assisted with $^{40}\text{Ar}/^{39}\text{Ar}$ incremental heating analyses. We thank Dr. Saeed Alshaltoni for assistance with sample collection and thin section preparation. R.A.D. acknowledges support from the Distinguished Scientist Fellowship Program at King Saud University.

BIBLIOGRAPHY

- Bohannon, R.G., C.W. Naeser, D.L. Schmidt, R.A. Zimmerman, (1989). The Timing of Uplift, Volcanism, and Rifting Peripheral to the Red Sea—a Case for Passive Rifting? *Journal of Geophysical Research*, 94, 1683-1701.
- Camp, V.E., and M.J. Roobol, (1992). Upwelling Asthenosphere Beneath Western Arabia and Its Regional Implications. *Journal of Geophysical Research*, 90, 15,255-15,271.
- Chang, S., and S. Van der Lee, (2011). Mantle Plumes and associated flow beneath Arabia and East Africa. *Earth and Planetary Science Letters*, 302, 448-454.
- Dalrymple, G.B., and M.A. Lanphere, (1969), Potassium-argon dating: W.H. Freeman and Company, San Francisco, 258 p.
- Duncan, R. A., A.M. Al-Amri, (2013). Timing and Composition of Volcanic Activity at Harrat Lunayyir, Western Saudi Arabia. *Journal of Volcanology and Geothermal Research*, 260, 103-116.
- Fitton, J.G., A.D. Saunders, M.J. Norry, B.S. Hardarson, and R.N. Taylor, (1997). Thermal and chemical structure of the Iceland plume. *Earth and Planetary Science Letters*, 153, 197–208.
- Ghiorso, M. S., and R.O. Sack, (1995). Chemical mass transfer in magmatic processes IV. A revised and internally consistent thermodynamic model for the interpolation and extrapolation of liquid-solid equilibria in magmatic systems at elevated temperatures and pressures. *Contributions to Mineralogy and Petrology*, 119(2-3), 197-212.
- Gurenko, A. A., and M. Chaussidon, (1995). Enriched and depleted primitive melts

- included in olivine from Icelandic tholeiites: origin by continuous melting of a single mantle column. *Geochimica et Cosmochimica Acta*, 59, 2905-2917.
- Kelley, K.A., R.H. Kingsley, and J.G. Schilling, (2013). Composition of Plume-Influenced Mid-Ocean Ridge Lavas and Glasses from the Mid-Atlantic Ridge, East Pacific Rise, Galapagos Spreading Center, and Gulf of Aden. *Geochemistry, Geophysics, Geosystems*, 14, 223-242.
- Koppers, A.A.P., (2002). ArArCALC - software for Ar-40/Ar-39 age calculations. *Computers & Geosciences*, 28(5), 605-619.
- McDonough, W. F. and S. S. Sun, (1989). Chemical and Isotopic Systematics of Ocean Basalts: Implications for Mantle Composition and Processes. *Geological Society, London, Special Publications*, 42, 313-345.
- Moufti, M.R.H, and M.H. Hashad, (2005). Volcanic Hazards Assessment of Saudi Arabian Harrats: Geochemical and isotopic Studies of Selected Areas of Active Makkah-Madinah-Nafud (MMN) Volcanic Rocks. Final Report (LGP-5-27). King Abdulaziz City for Science and Technology, Riyadh, Saudi Arabia.
- Murcia, H., J.M. Lindsay, S. Niedermann, S.J. Cronin, I.E.M. Smith, N.N. El-Masry, M.R.H. Moufti, K. Nemeth, (2013). The potential use of cosmogenic nuclides for dating in Harrat Rahat. *Vorisa Scientific Meeting*, 24-28.
- Pallister, J.S., (1984). Reconnaissance Geology of the Harrat Hutaymah Quadrangle, Sheet 26/42 A, Kingdom of Saudi Arabia: Ministry of Petroleum and Mineral Resources, Deputy Ministry for Mineral Resources, Jiddah, Kingdom of Saudi Arabia, Open-File Report USGS-OF_04-46, 77 p.
- Renne, P.R., C.C. Swisher, A.L. Deino, D.B. Karner, T.L. Owens, and D.J. DePaolo, (1998). Inrer calibration of Standards, Absolute Ages and Uncertainties in Ar-40/Ar-39 Dating. *Chemical Geology*. 145, 117-152
- Shaw, J.E., J.A. Baker, M.A. Menzies, M.F. Thirlwall, K.M. Ibrahim, (2003). Petrogenesis of the largest intraplate volcanic field on the Arabian Plate (Jordan): a mixed lithosphere–asthenosphere source activated by lithospheric extension. *Journal of Petrology*, 44, 1657–1679.
- Thornber, C.R., (1992). The Petrology, Geochemistry, and Origin of Ultramafic Inclusions and Mafic Alkaline Volcanics from Harrat Hutaymah, Saudi Arabia (Doctoral Dissertation). University of Colorado.
- Thornber, Carl R., (1990). Geologic map of Harrat Hutaymah, Saudi Arabia, with the petrologic classification and distribution of ultramafic inclusions (1:100,000 scale), USGS Miscellaneous Field Studies Map MF-2129.

Vlastelic, I., L. Dosso, H. Guillou, H. Bougault, L. Geli, J. Etoubleau, and J.L. Joron, (1998). Geochemistry of the Hollister Ridge: Relation with the Louisville Hotspot and the Pacific-Antarctic Ridge. *Earth Planet Science Letter*, 160, 777-793.